Supplementary Information

Spontaneous generation and active manipulation of real-space optical vortex

Dongha Kim[1*], Arthur Baucour[2], Yun-Seok Choi[3], Jonghwa Shin[2], and Min-Kyo Seo[1,3*]

[1]Department of Physics, KAIST, Daejeon 34141, Republic of Korea,

[2]Department of Materials Science and Engineering, KAIST, Daejeon 34141, Republic of Korea,

[3]Department of Chemistry, KAIST, Daejeon 34141, Republic of Korea,

*Corresponding author: dongha_kim@kaist.ac.kr, minkyo_seo@kaist.ac.kr

Supplementary Note 1. Origin of the non-trivial topological phase in the GTOC

Considering all possible optical paths, the multiple beam interference theory provides a thorough understanding of the generation and behaviour of the non-trivial topological phase in the reflection in the GTOC. As illustrated in Figure S1a, the GTOC consists of three optical interfaces: the air-SiO_2, SiO_2-Ni, and SiO_2-Al interfaces. The Ni layer functions as a partial reflector and makes the top and bottom SiO_2 layers act as coupled resonators. Here, r_A (r_A'), r_{Ni}, and r_B are the reflection coefficients at the air-SiO_2 (SiO_2-air), SiO_2-Ni, and SiO_2-Al interfaces. t_A (t_A'), and t_{Ni} are the transmission coefficients at the air-SiO_2 (SiO_2-air) and SiO_2-Ni interfaces. The reflection and transmission coefficient at air-SiO_2 interface satisfy the Stokes relations, $t_A t_A' = 1 - r_A^2$ and $r_A' = -r_A$. As illustrated in Figures S1b and S1c, the optical paths contributing to the total reflection coefficient (r) are categorised into two groups: 1) the optical paths including the propagation only above the Ni layer (r_1) and 2) the other paths including the transmission through the Ni layer (r_2).

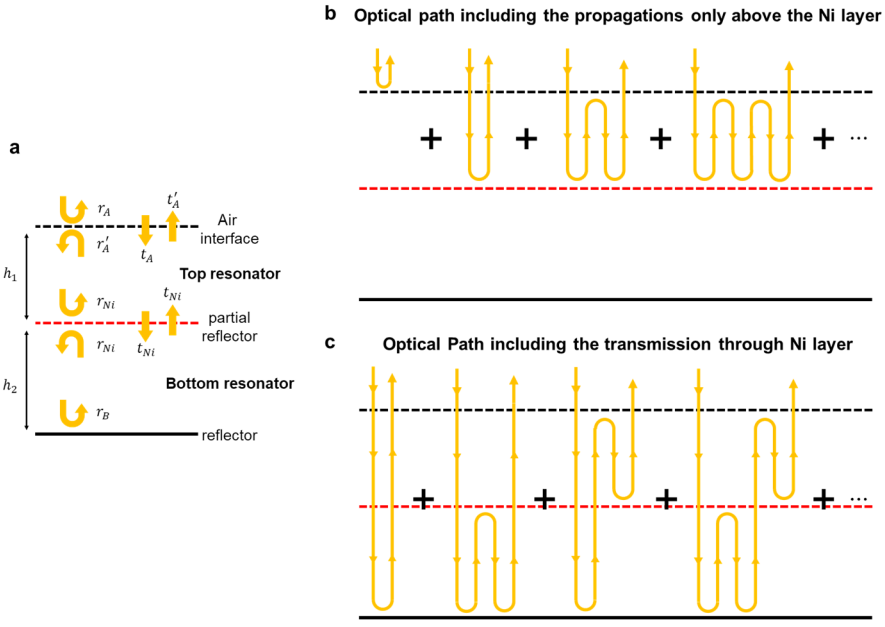

Figure S1. (a) Schematic of the optical paths in the GTOC. **(b)** Optical paths including the propagation only above the Ni layer. **(c)** Optical paths including the transmission through the Ni layer.

The contribution of each group (r_1 and r_2) is derived by the sum of the series of all related paths:

$$
\begin{aligned}
r_1 &= \sum (\text{paths including propagation only above Ni layer}) \\
&= r_A + t_A t_A' r_{Ni} e^{-i\phi_1} + t_A t_A' r_{Ni} e^{-i\phi_1} r_A' r_{Ni} e^{-i\phi_1} + t_A t_A' r_{Ni} e^{-i\phi_1} \left(r_A' r_{Ni} e^{-i\phi_1}\right)^2 + \cdots \\
&= r_A + (1 - r_A^2) r_{Ni} e^{-i\phi_1} \frac{1}{1 + r_A r_{Ni} e^{-i\phi_1}}
\end{aligned}
$$

$$
\begin{aligned}
r_2 &= \sum (\text{paths including transmission through Ni layer}) \\
&= t_1 t_1' t_{Ni}^2 r_2 e^{-i\phi_1} e^{-i\phi_2} + t_1 t_1' t_{Ni}^2 r_{Ni} r_2^2 e^{i\phi_1} \left(e^{i\phi_2}\right)^2 + t_1 t_1' r_1' t_{Ni}^2 r_{Ni} r_2 \left(e^{i\phi_1}\right)^2 e^{i\phi_2} + \cdots \\
&= r - r_1
\end{aligned}
$$

where $\phi_{1(2)} = \frac{2\pi}{\lambda} n_{SiO_2} h_{1(2)}$, n_{SiO_2} is the refractive index of SiO_2, and λ is the wavelength of light. The total reflection coefficient (r) is given by $r_1 + r_2$ and can also be calculated by the transfer matrix method.

The generation of optical vortex and antivortex requires a topological texture with a zero-intensity singular point. When the Ni layer has an appropriate thickness (from 6.29 to 13.15 nm), the GTOC allows complete destructive interference between the optical fields in the top and bottom SiO_2 resonators: $r = r_1 + r_2 = 0$. In Figure S2a and S2b, we plotted the amplitude and phase distribution of the calculated reflection coefficient components (r_1 and r_2) in the generalised parameter space (h_1, h_2). The yellow and green solid curves represent the same amplitude ($|r_1| = |r_2|$) and out-of-phase conditions ($\arg(r_1) = \arg(-r_2)$), respectively. As shown in Figure S2c, in the GTOC of in h_{Ni} = 10 nm, the same amplitude and out-of-phase conditions intersect each other, and thus, the complete destructive interference with a singular minimum of reflection is established. The winding direction of the difference between $\arg(r_1)$ and $\arg(r_2)$ determines the topological charge of the singular minimum at the intersection; The red and blue dots indicate the optical vortex ($w = +1$) and antivortex ($w = -1$), respectively. On the other hand, in the GTOCs of h_{Ni} = 5 and 15 nm, the same amplitude and out-of-phase conditions do not have any interconnection. We note that the same amplitude and out-of-phase conditions appear as a closed loop and a finite curved line, respectively, in the whole area of the GTOC unit cell (See Supplementary Movie 1). The evolution of those conditions depending on h_{Ni} clarifies the origin of the topological phase transition from trivial to non-trivial and vice versa.

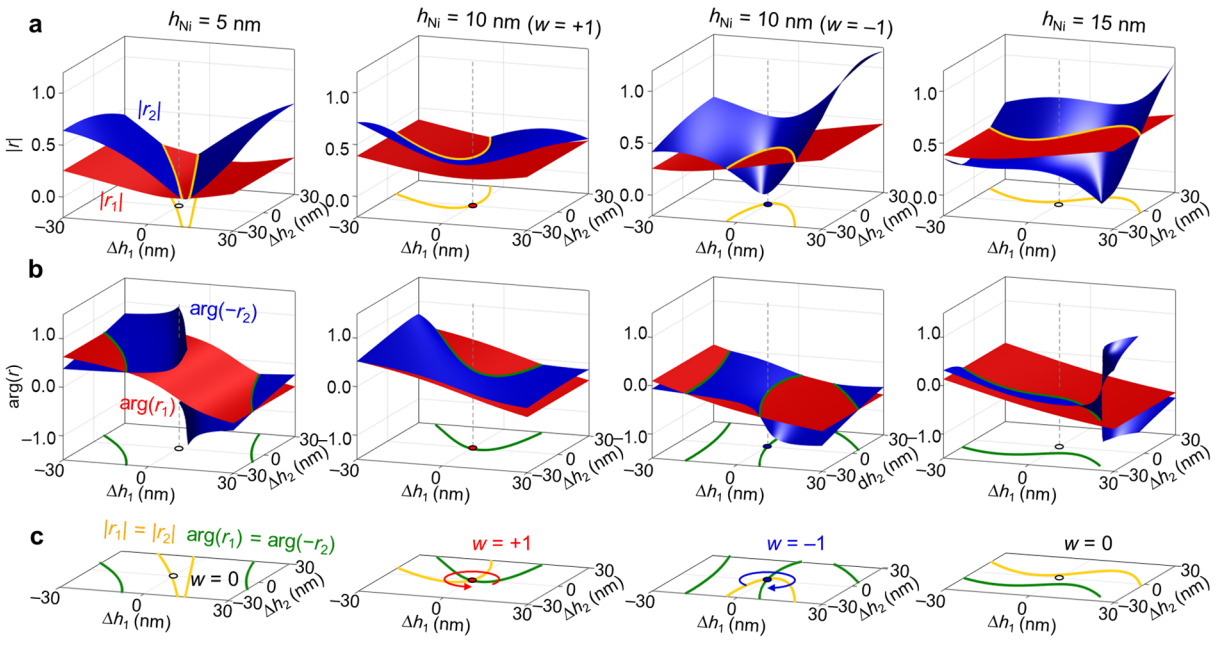

Figure S2. (a,b) Plot of the (a) amplitude and (b) phase of the reflection coefficient components r_1 (the red curved surface) and r_2 (the blue curved surface) near the reflection minima in the generalised parameter space for the GTOCs with h_{Ni} = 5, 10, and 15 nm. (Δh_1, Δh_2) represents the position away from the target reflection minimum in the generalised parameter space. The yellow and green solid curves represent the same amplitude ($|r_1| = |r_2|$) and out-of-phase conditions ($\arg(r_1) = \arg(-r_2)$), respectively. **(c)** Projection of the same amplitude (the yellow curve)

and out-of-phase (the green curve) conditions onto the generalised parameter space. The singular minimum of reflection for the non-trivial topological textures exists only when the two conditions intersect. The red and blue dots indicate the intersections for the optical vortex ($w = +1$) and antivortex ($w = -1$), respectively. The white circles indicate the positions of the weak reflection minima of the trivial topological phase ($w = 0$).

Supplementary Note 2. Thickness distribution and gradient in the SiO_2 layer

We experimentally investigated the thickness spatial distribution of the SiO_2 layers deposited by radio-frequency (RF) sputtering. As illustrated in Figure S3a, we loaded 17 pieces of 1×1-cm^2-sized Si substrate simultaneously and checked the thickness of the deposited SiO_2 layer depending on the orientation and position with respect to the centre of the sample holder. We measured the thickness of the SiO_2 layer at the centre of the sample by spectroscopic ellipsometry (J. A. Woollam alpha-SE) (Figure S3b). The thickness of the SiO_2 layer exhibits a parabolic-like distribution and decreases as the location moves away from the centre of the sample holder. We extracted the two-dimensional thickness distribution of the deposited SiO_2 layer in our machine by applying a polynomial fit on the measured data (Figure S3c). We note that the point of maximum deposition thickness is slightly displaced from the centre of the sample holder. The demonstrated GTOCs were fabricated in the region of 2×2 cm^2 (indicated by the black dashed box in Figure S3c), of which the centre is ~3 cm away from the point of maximum deposition. As shown in Figure S3d, the SiO_2 layer thickness varies by ~41.33% from its maximum value over the employed region, which covers a sufficiently large area in the generalised parameter space (h_1, h_2) to investigate the topological textures in this study.

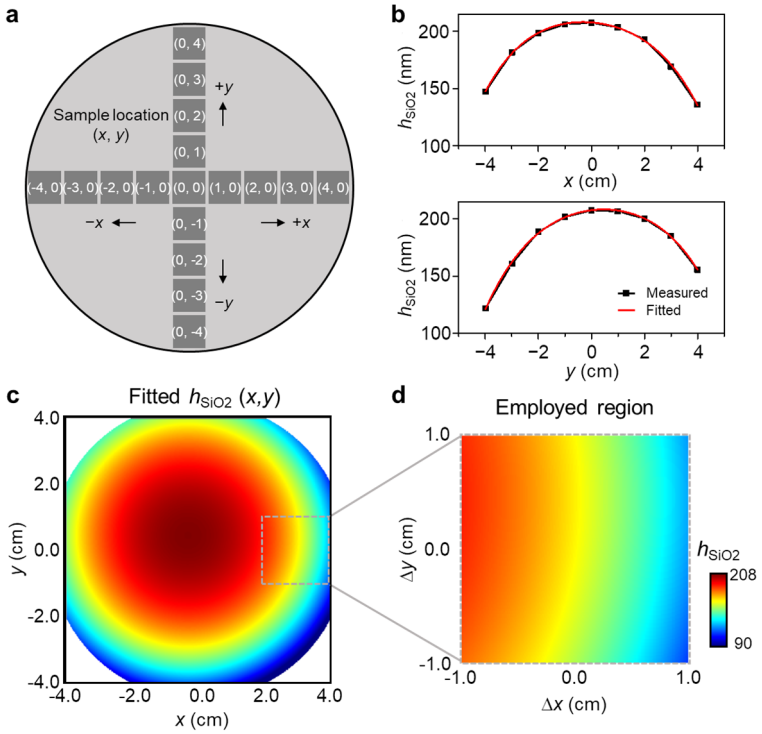

Figure S3. Measurement of the thickness distribution of the deposited SiO_2 layer depending on the position and orientation in the sample holder of the employed RF sputtering machine. (a) Illustration of the loaded Si samples on the sample holder. **(b)** Measured (black squares) and fitted (solid red line) thickness of the SiO_2 layer depending on the position in the horizontal (x-axis) and vertical (y-axis) directions. **(c)** Extracted two-dimensional SiO_2 thickness distribution in the xy plane over the sample holder. The dashed box indicates the area used in the fabrication of the GTOC samples. **(d)** Magnification of the SiO_2 layer thickness distribution in the region employed in fabrication.

We also confirmed that the normalised spatial distribution of the SiO_2 layer thickness remains the same, regardless of the final deposition thickness (Figure S4). We examined two different deposition sets of which the central sample (x = 0 cm) has a final thickness of 76 nm and 145 nm, respectively (Figure S4a). As shown in Figure S4b, the normalised distributions of the two sets are identical, which verifies the consistency of the sputtering deposition process for the thickness gradient SiO_2 layer. Therefore, the normalised distribution of the SiO_2 layer thickness in Figure S3d allows precise bijective projection between the real and generalised parameter spaces shown in Figures 2a and 2b in the main manuscript.

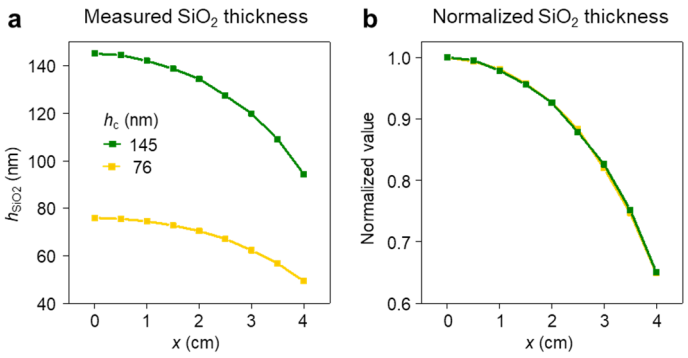

Figure S4 Consistency of the sputtering deposition process for the thickness gradient SiO_2 layer. **a,** Measured thickness of the SiO_2 layer depending on the position for two different deposition sets. Each set consists of nine samples at different horizontal positions from x = 0 cm to 4 cm and has a final thickness (h_c) of the central sample (x = 0 cm) of 76 nm and 145 nm, respectively. **b,** Normalised distribution of the SiO_2 layer thickness.

The ellipsometry results yield the spatial thickness distributions of the top and bottom SiO_2 layers over the GTOC sample (Figure S5). We were thus able to perform the bijective projection between the real and generalized parameter spaces (see also Figure 2b in the main manuscript).

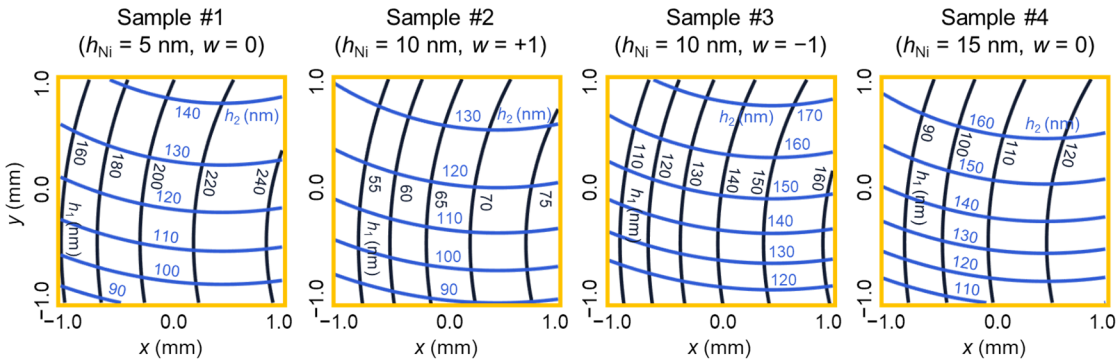

Figure S5 Thickness distributions of the top and bottom SiO_2 layers (h_1 and h_2) of the four GTOC samples (Sample #1, #2, #3, and #4 in the main manuscript). The black and blue lines indicate the equal-thickness curves of the top and bottom SiO_2 layers.

Supplementary Note 3. Extraction of the complex reflection coefficient distribution

Off-axis holography measures the interferogram of the target sample to obtain the complex reflection coefficient distribution [1]. Figure S6a illustrates the employed off-axis holography setup for interferometric imaging, in which the reflected light from the sample interferes with the oblique reference beam from the slightly tilted mirror (~1°). The interferogram exhibits intensity oscillations along the tilted direction of the reference mirror and, especially when an optical vortex exists, has the well-known fork pattern.

Figure S6b shows the step-by-step extraction process of the complex reflection coefficient distribution from the measured interferogram as follows:

(1) Fourier transform of the measured interferogram $I(x, y)$
(2) Crop of the interference signal from the Fourier transformed interferogram $I(k_x, k_y)$
(3) Shift of the cropped interference signal $I_{crop}(k_x, k_y)$ to the centre of the Fourier space
(4) Inverse Fourier transform to retrieve the complex reflection coefficient distribution

The Fourier transformed interferogram possesses three intensity peaks: one central peak and two side peaks. The interference signal around the side peak contains the holographic information of the reflected light from the target sample. The peak at the centre just gives the intensity sum of the reflected light from the target sample and the reference beam. Shifting the interference signal at the centre of the Fourier space, we can extract the complex reflection coefficient distribution solely without intensity oscillations originating from the oblique incidence of the reference beam.

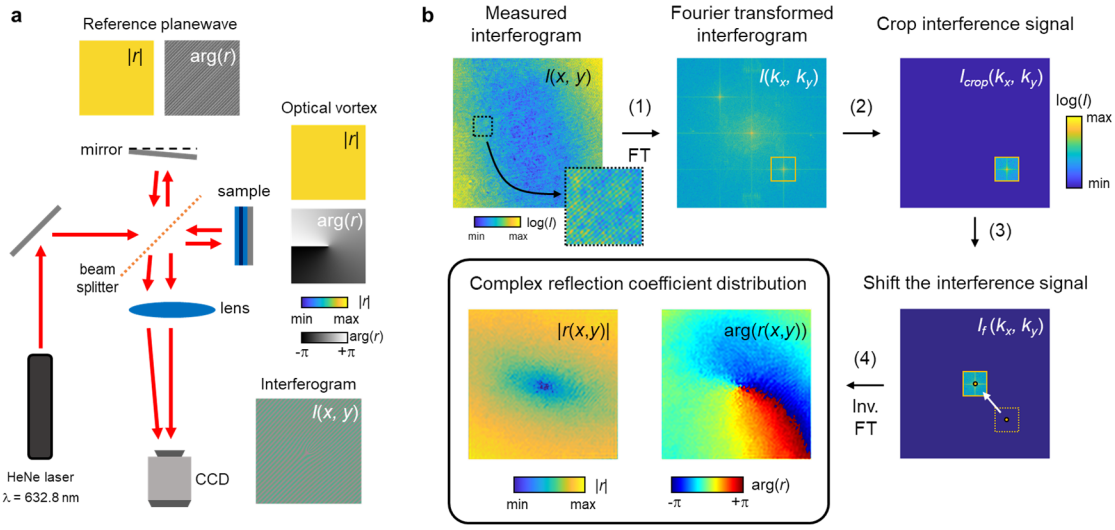

Figure S6. (a) Schematic of the off-axis holography set-up for interferometric imaging. **(b)** Step-by-step extraction process of the complex reflection coefficient distribution. Here, we present the case of Sample #2 supporting the optical vortex. The magnified measured interferogram (the dashed box) clearly shows intensity oscillations due to the interference with the obliquely incident reference beam. The yellow box indicates the cropped area for the interference signal in the Fourier space.

[1] Etienne Cuche, Pierre Marquet, and Christian Depeursinge, "Spatial filtering for zero-order and twin-image elimination in digital off-axis holography," *Applied Optics*, **39** 4070-4075 (2000)

Supplementary Note 4. Trivial topological textures under external magnetic field

The non-trivial topological textures, supporting the optical vortex and antivortex, exhibit the effective spin-orbit interaction depending on their non-zero topological charge ($w = \pm 1$), as shown in Figure 3 in the main manuscript. However, the trivial topological textures, supporting a weak reflection minimum with a zero-topological charge ($w = 0$), do not show such a unique, dynamic interaction with the magnetisation governed by the external magnetic field. Figure S7 shows the behaviours of the weak reflection minimum in the trivial topological phase (Sample #1 and #4), depending on the external magnetic field. We measured the complex reflection coefficient for the right-handed (+σ) circularly-polarised light. Showing that the position of the weak reflection minimum is static, the reflection amplitude was barely changed by the external magnetic field. The external magnetic field does not cause any local change or dynamic behaviour in the reflection phase distribution either.

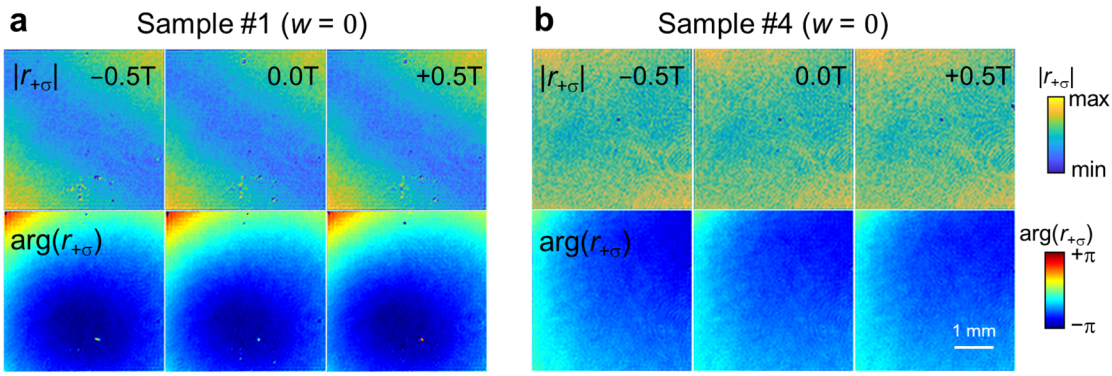

Figure S7. External magnetic field-dependent behaviour of the complex reflection coefficient ($r_{+\sigma}$) of the trivial topological textures that **(a)** Sample #1 and **(b)** #4 (the GTOCs of h_{Ni} = 5 nm and 15 nm in Figure 2 in the main manuscript) support, respectively.

Supplementary Note 5. Optical vortex dynamics with complex magneto-optic parameter

The consideration of the complex nature of the magneto-optic parameter of Ni offers further analysis of the effective spin-orbit interaction of the optical vortex and antivortex in the GTOC. The magneto-optic effects in transition metals arise circular birefringence in which the refractive index for the right-handed (+σ) and left-handed (−σ) circularly-polarised light is given as $n_{\pm\sigma}^2 = \varepsilon_{\mathrm{Ni}}(1 \pm Q_{\mathrm{Ni}})$. Here, $\varepsilon_{\mathrm{Ni}}$ and Q_{Ni} is the optical permittivity and Voigt parameter of the magnetised Ni layer, respectively. The optical thickness of the Ni layer thus becomes $\mathrm{Re}\{n_{\pm\sigma}h_{\mathrm{Ni}}\}$ where ϕ_{Ni} is the argument of the Voigt parameter as $Q_{\mathrm{Ni}} = Q_0 e^{-i\phi_{\mathrm{Ni}}}$. When Q_{Ni} is real ($Q_{\mathrm{Ni}} = Q_0$), the effective change of h_{Ni} by the external magnetic field is described as $h_{\mathrm{Ni}}\sqrt{1+Q_0}$ for the right-handed circularly-polarised light. In the main manuscript, the effective change of h_{Ni} was estimated to be ~0.06 nm in Sample #2 and ~0.05 nm in Sample #3, by fitting the measured vortex/antivortex movements in Figures 3e and 3f to the theoretical calculations in Figure 3b.

The magneto-optic effects in fact cause the complex-valued effective change on the Ni layer given as $n_{\pm\sigma}h_{\mathrm{Ni}}\sqrt{1 \pm Q_0 e^{-i\phi_{\mathrm{Ni}}}}$ and thus provide the optical vortex and antivortex with an additional spatial degree of freedom in their dynamics. In Figure S8, we calculated the movement of the optical vortex and antivortex in the GTOC with a 10-nm-thick Ni layer depending on ϕ_{Ni} in the generalised parameter space of (h_1, h_2), where h_1 and h_2 are the thicknesses of the top and bottom SiO_2 layers. The change of ϕ_{Ni} allows the optical vortex and antivortex to move in any direction in the generalised parameter space other than the trajectory determined by the solutions of the nontrivial singular zero-reflection for a given h_{Ni}. We also plotted the measured trajectories of the optical vortex and antivortex depending on the applied magnetic field in the generalised parameter space (Figures 3e and 3f in the main manuscript show the trajectories in the real space).

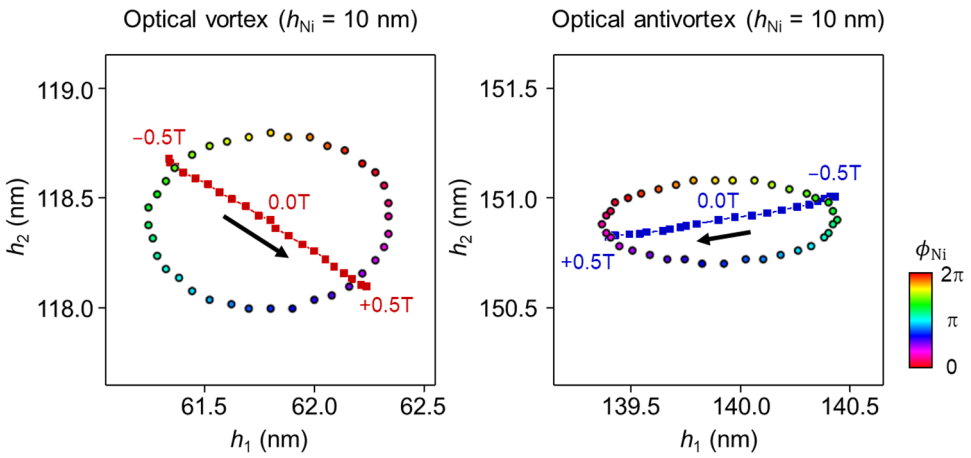

Figure S8. Movements of the optical vortex and antivortex in the generalized parameter space depending on the argument (ϕ_{Ni}) of the Voigt parameter. The HSV colour circles indicate the calculated movements of the optical vortex/antivortex from its initial position for the non-magnetised 10-nm-thick Ni layer depending on ϕ_{Ni}. The red and blue squares are the bijective projection of the experimentally measured trajectories of the optical vortex and antivortex (Figures 3e and 3f in the main manuscript) onto the generalised parameter space.

Supplementary Note 6. Fork interferogram of optical vortex and antivortex

Optical vortices can be effectively identified and characterised by the fork patterns in the holographic interferogram. In the original interferogram, as measured by the off-axis holography setup, the fork pattern is buried in the intensity oscillations of which the spatial frequency is too fast and cannot be resolved well by the employed imaging camera (Figure S6). The spatial frequency of intensity oscillations can be controlled as desired by changing the tilt angle of the reference mirror experimentally or adding a continuously varying global phase to the measured reflection phase distribution mathematically. In this work, we added a continuously varying global phase by locating the cropped interference signal $I_{crop}(k_x, k_y)$ away from the centre of the Fourier space as shown in Figure S9 and obtained the fork interferograms in Figure 4b in the main manuscript.

Figures S9a and S9b show how the fork interferogram of the ideal optical vortex changes as the position of the cropped interference signal (k_{xc}, k_{yc}) moves from (0, 0) to $(15\Delta k, 15\Delta k)$. Here, Δk is the resolution of the discrete Fourier transform. The fork interferogram of the complex reflection coefficient distribution is obtained by the inverse Fourier transform of the shifted interference signal. The continuously varying global phase employed here causes the fork's head to point the right-downward (left-upward) direction for the optical vortex (antivortex), as shown in Figure S9c. Figure S9d shows the obtained fork interferogram of the optical vortex-antivortex pair in Sample #5 under the applied magnetic field of 0.5 T. Note that, the employed shifting condition here is $(8\Delta k, 8\Delta k)$.

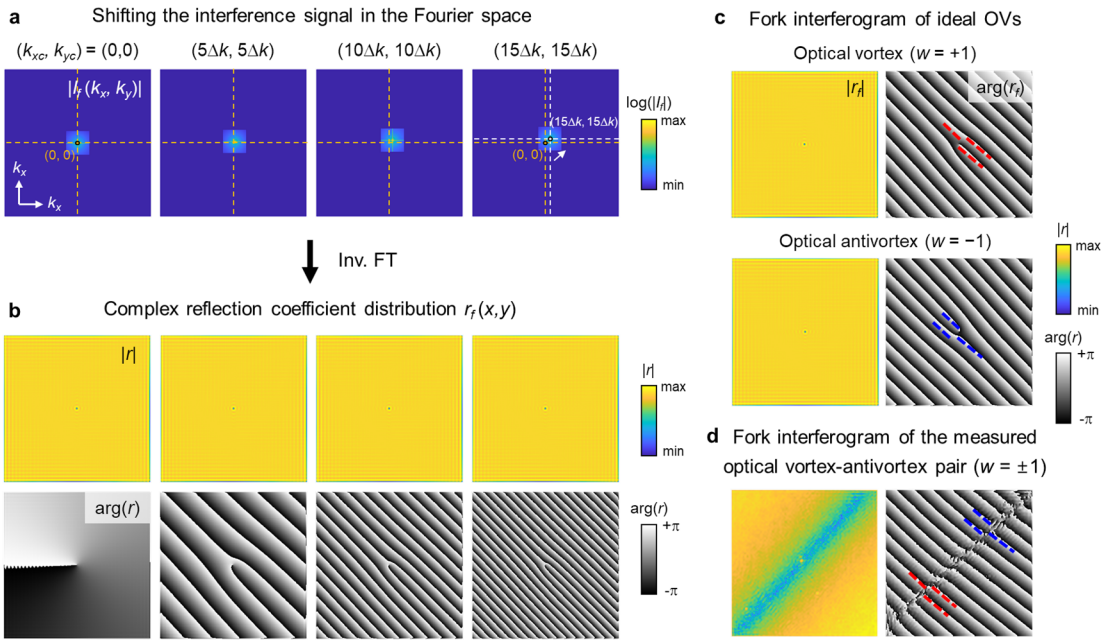

Figure S9. Extraction of the fork interferogram. (a) Shift of the interference signal in the Fourier space to a continuously varying global phase. **(b)** Fork interferogram of the ideal optical vortex depending on the shift of the interference signal in the Fourier space. **(c)** Calculated fork interferogram of the ideal optical vortex and antivortex. **(d)** Fork interferogram of the optical vortex-antivortex pair created in Sample #5 at B = 0.5T (See also Figure 4 in the main manuscript).